


Anomalous hybridization of spectral winding topology in quantized steady-state responsesHui-Qiang Liang ¹, Sen Mu,^{2,*} Jiangbin Gong,^{2,†} and Linhu Li ^{1,‡}¹*Guangdong Provincial Key Laboratory of Quantum Metrology and Sensing and School of Physics and Astronomy, Sun Yat-Sen University, Zhuhai 519082, China*²*Department of Physics, National University of Singapore, Singapore 117551, Republic of Singapore*

(Received 3 January 2022; revised 6 April 2022; accepted 16 May 2022; published 2 June 2022)

The quantized response is one distinguishing feature of a topological system. In non-Hermitian systems, the spectral winding topology yields a quantized steady-state response. By considering two weakly coupled non-Hermitian chains, we discover that the spectral winding topology of one chain can be probed by a steady-state response defined solely on the other chain, even when other important properties, e.g., energetics and entanglement entropy, indicate that eigensolutions are effectively not hybridized between the two chains. This intriguing phenomenon, as carefully investigated in a large parameter space with a varying system size, not only offers a different angle to understand interchain signal propagation in a non-Hermitian setting but also reveals unexpected physics of spectral winding topology vs quantized response.

DOI: [10.1103/PhysRevB.105.L241402](https://doi.org/10.1103/PhysRevB.105.L241402)**I. INTRODUCTION**

Rooted in complex eigenenergies, the spectral winding topology of non-Hermitian systems constitutes a new aspect of topological physics with no Hermitian counterpart [1–5]. Spectral winding is critical to predict the seminal non-Hermitian skin effect (NHSE), as characterized by the localization of all eigenmodes at the boundary of the system [1–17]. Nontrivial spectral winding has also been experimentally observed in various platforms, including an optical ring resonator with electro-optic modulators [18], an acoustic crystal [19], and a hybrid light-matter system [20]. Besides localized boundary states, a quantized response is a characteristic feature of topological systems, e.g., the quantized conductance in the celebrated quantum Hall effect. Recently, a quantized steady-state response, namely, the response to a driving field of a nonequilibrium system when it reaches steady conditions, is established to further manifest the spectral winding topology in non-Hermitian chains, where a quantity defined from the response to a driving field is found to be quantized and matched exactly with the spectral winding number [21].

Spectral winding is usually investigated under periodic boundary conditions (PBCs), because it is simply prohibited under open boundary conditions (OBCs) [4,5]. Near or at the limit of OBCs, other properties of non-Hermitian systems may change drastically upon tuning of an extremely weak boundary coupling [22–25] or a coupling between two chains with dissimilar skin localizations [26–28]. Such hypersensitivity to weak perturbations are of continued interest, especially in connection with sensor designs [22–31]. Under intermediate boundary conditions between PBCs and OBCs, some aspects of the complex spectrum and eigenmode

localization characteristics were also studied [11,12,24,25]. This work investigates another problem, namely, how spectral winding features, as manifested in the quantized steady-state response, react to weak interchain coupling when a system is not under PBCs or OBCs.

Specifically, in examining quantized steady-state responses in connection with the spectral winding topology of two weakly coupled non-Hermitian chains, we discover a so-called anomalous hybridization regime. In this regime, on the one hand, the eigensolutions are effectively not hybridized between the two chains in many aspects; e.g., with vanishing entanglement between the two chains, quantized steady-state responses can be observed on either chain without complications due to the other. On the other hand, the spectral winding topology associated with one chain can be captured through a response defined solely on the other chain, indicating a nontrivial hybridization. Such a counterintuitive phenomenon is explained by considering the propagation channels between the two chains under resonance conditions. We then carefully investigate the transitions of the system between dehybridization, anomalous hybridization, and strong hybridization regimes, through different quantized steady-state responses as well as an entanglement entropy analysis. Significantly, the regime of anomalous hybridization, which is of most interest here, occurs in a relatively large parameter space, with the allowed interchain coupling much stronger than that which yields critical behaviors for systems initially under OBCs [26]. Our extensive computational results show that this regime further widens when increasing the system's size, indicating that the physics of anomalous hybridization uncovered here is even more typical in the thermodynamic limit.

II. MODEL

We consider the probing response on two weakly coupled Hatano-Nelson chains [32] with different asymmetric

* senmu@u.nus.edu

† phygj@nus.edu.sg

‡ lilh56@mail.sysu.edu.cn

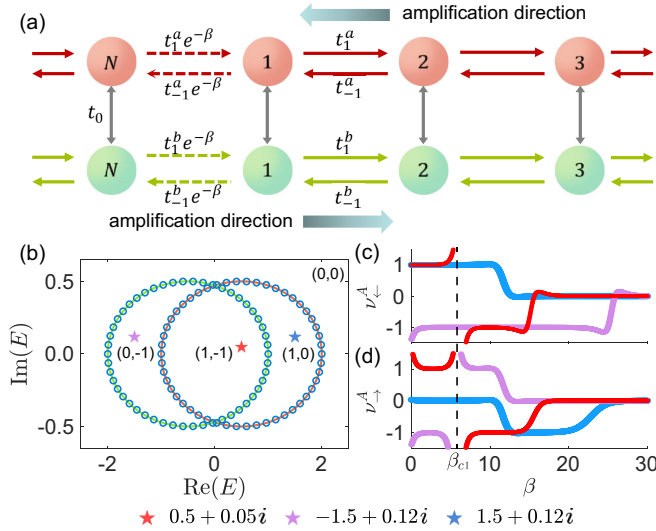


FIG. 1. (a) Sketch of the coupled-chain system. (b) PBC spectra of the system with $t_0 = 10^{-2.5}$ (blue circles) and $t_0 = 0$ (colored loops), which are almost on top of each other. The spectral winding numbers $\mathbf{w}(E_r) = (w_+(E_r), w_-(E_r))$ for E_r in different regions are indicated in the figure. (c) and (d) Quantized steady-state response quantities defined on chain A (at $t_0 = 10^{-2.5}$) for the three chosen points labeled by stars with different colors in (b). The other parameters are $N = 50$, $t_1^A = t_{-1}^A = 1$, $t_{-1}^B = t_1^B = 0.5$, and $V^A = -V^B = 0.5$.

nearest-neighbor hoppings, as shown in Fig. 1(a). The model system is described by the tight-binding Hamiltonian

$$\begin{aligned} \hat{H} = & \sum_{\alpha=A,B} \sum_{x=1}^{N-1} (t_1^\alpha \hat{c}_{x,\alpha}^\dagger \hat{c}_{x+1,\alpha} + t_{-1}^\alpha \hat{c}_{x+1,\alpha}^\dagger \hat{c}_{x,\alpha}) \\ & + \sum_{x=1}^N \left(t_0 \hat{c}_{x,A}^\dagger \hat{c}_{x,B} + t_0 \hat{c}_{x,B}^\dagger \hat{c}_{x,A} + \sum_{\alpha=A,B} V^\alpha \hat{c}_{x,\alpha}^\dagger \hat{c}_{x,\alpha} \right) \\ & + e^{-\beta} \sum_{\alpha=A,B} (t_1^\alpha \hat{c}_{N,\alpha}^\dagger \hat{c}_{1,\alpha} + t_{-1}^\alpha \hat{c}_{1,\alpha}^\dagger \hat{c}_{N,\alpha}), \end{aligned} \quad (1)$$

with $c_{x,\alpha}^\dagger$ the creation operator at the x -lattice site on chain α , $t_{\pm 1}^\alpha$ the asymmetric hopping amplitudes, V^α the on-site potential in chain α , and t_0 the interchain coupling at each lattice site. A realization of this model using cavity arrays is discussed in Sec. VII and the Supplemental Material [33] (which contains Refs. [34–36]). When $t_0 = 0$, the non-Hermitian asymmetric hoppings of each chain leads to a directional amplification of a signal entering the system [37–39], and in the following discussion we will mainly focus on cases with the two chains having opposite amplification directions [as indicated in Fig. 1(a)]. The boundary conditions in this model can be tuned from PBCs to OBCs by increasing β from 0 to infinity. Under PBCs, i.e., $\beta = 0$, the Bloch Hamiltonian is given by

$$h(k) = \begin{pmatrix} 2t^A \cos(k - i\eta_A) + V^A & t_0 \\ t_0 & 2t^B \cos(k - i\eta_B) + V^B \end{pmatrix}, \quad (2)$$

with k the quasimomentum, $\eta_{A/B} = \ln \sqrt{t_1^{A/B}/t_{-1}^{A/B}}$ the non-Hermitian inverse localization length, and $t^{A/B} = \sqrt{t_1^{A/B} t_{-1}^{A/B}}$. For either $\eta_{A/B} \neq 0$, the Hamiltonian is non-Hermitian and point gapped with a topological winding number defined with respect to a reference energy E_r in the complex energy plane,

$$w(E_r) = w_+(E_r) + w_-(E_r), \quad (3)$$

with

$$w_\pm(E_r) = \int_{-\pi}^{\pi} \frac{dk}{2\pi i} \partial_k \ln[E_\pm(k) - E_r] \quad (4)$$

the single-band spectral winding numbers, \pm the band index, and $E_\pm(k)$ the complex eigenenergies of the Hamiltonian.

Figure 1 depicts the PBC spectrum of our system and its corresponding two-component winding numbers

$$\mathbf{w}(E_r) = (w_+(E_r), w_-(E_r)).$$

Assuming an ultraweak interchain coupling $t_0 \ll t^\alpha$, it is possible that the eigensolutions of Eq. (2) are effectively not hybridized between the two chains. Note that the two bands are seen to cross each other in the complex plane, yet we have $E_+(k) \neq E_-(k)$ for every lattice momentum k [40]; thus the notion of energy bands can still be well defined. As seen in Fig. 1(b), the two PBC bands with a small t_0 are virtually identical to the spectrum of the two uncoupled chains, respectively. We simply have $\mathbf{w}(E_r) = (w_A(E_r), w_B(E_r))$ at $t_0 = 0$. As such, the single-band winding number $w_+(E_r)$ [$w_-(E_r)$] is expected to reflect only the spectral winding topology of chain A (B) under a weak interchain coupling. The complex energy plane is hence divided into four regimes, corresponding to different combinations of single-band winding numbers, respectively.

III. ANOMALOUS HYBRIDIZATION REGIME

To physically manifest the spectral winding topology, we consider steady-state responses in a directional signal amplification process [21]. The quantized coefficient is established by taking derivatives of a quantity involving the Green's function with respect to the boundary tuning parameter β ,

$$v_{\leftarrow}^\alpha(E_r) = d \ln |G_{\alpha 1, \alpha N}| / d\beta, \quad v_{\rightarrow}^\alpha(E_r) = d \ln |G_{\alpha N, \alpha 1}| / d\beta, \quad (5)$$

with α representing either of the two chains and $G_{\alpha x, \alpha x'}$ an element of the Green's function

$$G = 1/(E_r - H)$$

associated with the x th and x' th sites in chain α . Further, $G_{\alpha x, \alpha x'}$ can describe a signal amplification between two sites on the same chain [21, 37–39]. The reference energy can be expressed as

$$E_r = \omega + i\gamma,$$

with ω the frequency of an input signal and γ an extra uniform gain or loss adding to the system. According to early results of quantized steady-state responses vs spectral winding topology on a single chain [21], one expects to have $v_{\leftarrow}^\alpha(E_r) = w(E_r)$ for $w(E_r) = 1$ or $v_{\rightarrow}^\alpha(E_r) = -w(E_r)$ for $w(E_r) = -1$. These

coefficients will be nonpositive otherwise, e.g., $v_{\rightarrow}^{\alpha}(E_r) \leq 0$ for $w(E_r) = 1$, and always zero for large enough β when the response itself becomes constant¹.

We investigate the response on chain A alone for our system. Indeed, we obtain a plateau at $v_{\leftarrow}^A = 1$ and nonpositive v_{\rightarrow}^A when E_r falls in the region with $\mathbf{w}(E_r) = (1, 0)$ [e.g., the blue star in Fig. 1(b)], as shown by the blue lines in Figs. 1(c) and 1(d). This result is identical to the case when eigensolutions are not hybridized. Next, for E_r with $\mathbf{w}(E_r) = (0, -1)$ [e.g., the purple star in Fig. 1(b)], we see nonpositive v_{\leftarrow}^A in Fig. 1(c), and a plateau at $v_{\rightarrow}^A = 1$ in Fig. 1(d) appears only after the boundary tuning parameter β exceeds a certain value β_{c1} . This tells us that the response v_{\rightarrow}^A defined on chain A can only reflect the spectral winding related to chain B when $\beta > \beta_{c1}$, since negative winding is contributed from chain B . It should not be taken as a violation of the correspondence between winding topology and quantized steady-state response when $\beta < \beta_{c1}$, because here the response function is defined on chain A only (instead of involving both chains). We thus do not expect it to predict the total winding number or $w_{-}(E_r)$ (from chain B) immediately away from the PBCs, when the eigensolutions are effectively not hybridized between the two chains yet. In other words, $w_{-}(E_r)$ inherits the spectral winding topology of chain B only and is not captured by the response v_{\rightarrow}^A defined on chain A for E_r with $\mathbf{w}(E_r) = (0, -1)$ unless the eigensolutions are hybridized when $\beta > \beta_{c1}$. This seems to suggest that the eigensolutions in our system undergo a sharp transition from not hybridized to hybridized at $\beta = \beta_{c1}$, and we will justify this conjecture from entanglement analysis between the two chains later.

Now let us consider E_r falling in the central region with $\mathbf{w}(E_r) = (1, -1)$ [e.g., the red star in Fig. 1(b)]. First, as seen in Fig. 1(c), v_{\leftarrow}^A shows a plateau at $v_{\leftarrow}^A = 1$ when $\beta < \beta_{c1}$, in agreement with the single-band winding number $w_{+}(E_r) = 1$. For $\beta > \beta_{c1}$, v_{\leftarrow}^A drops to nonpositive values due to hybridization of the eigensolutions, also in agreement with a total winding number $w(E_r) = 0$ for the entire system. Surprisingly, unlike for E_r with $\mathbf{w}(E_r) = (0, -1)$, we find that the response v_{\rightarrow}^A now gives rise to a plateau at $v_{\rightarrow}^A = 1$ for $\beta < \beta_{c1}$, as shown by the red line in Fig. 1(d). This is unexpected since a positive v_{\rightarrow}^A reflects a negative winding number, which originates only from chain B in our system. This reveals that the response v_{\rightarrow}^A defined on chain A can reflect the spectral winding topology of chain B for E_r with $\mathbf{w}(E_r) = (1, -1)$, though the eigensolutions are effectively not hybridized between the two chains when $\beta < \beta_{c1}$ in our model. Our results uncover another subtle aspect of coupled non-Hermitian chains: It is highly nontrivial to tell how the eigensolutions cooperate in the steady-state response even when the interchain coupling is weak. Specifically, with several aspects in our system resembling those of dehybridized eigensolutions, a response defined on one chain can reveal the winding topology of the other for a certain frequency of the input signal, clearly indicating a hybridization behavior. To highlight this dual feature of dehybridization or hybridization

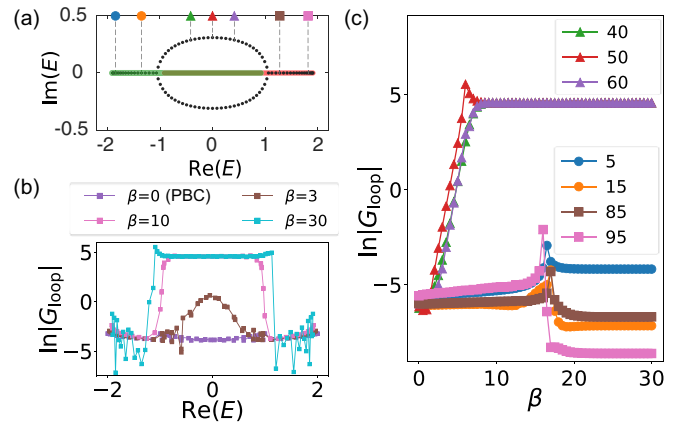


FIG. 2. (a) OBC spectra with $t_0 = 0$ (colored) and $t_0 = 10^{-2.5}$ (black). Red and green correspond to the spectra of two uncoupled chains, respectively, overlapping in the central part of the spectrum. (b) Plot of $G_{\text{loop}} = G_{A_x, B_{x'}} G_{B_{x'}, A_x}$ for reference energy E_r chosen as eigenenergies of the system with a small imaginary energy detuning in calculating the Green's function. The parameters are $N = 50$, $x = 20$, and $x' = 30$. (c) Plot of $\ln|G_{\text{loop}}|$ for several different eigenenergies labeled in (a) with the same symbols and colors. The legend shows the orders of the eigenenergies sorted in their real parts. The parameters are the same as in Fig. 1.

in different measures, we refer to it as anomalous hybridization hereafter. Similar behaviors are also seen in interchain response functions, associated with $G_{\alpha N, \bar{\alpha} 1}$ and $G_{\alpha N, \bar{\alpha} 1}$, where $\alpha \neq \bar{\alpha}$, as shown in the Supplemental Material [33].

IV. PROPAGATION CHANNELS BETWEEN TWO COUPLED CHAINS

The seemingly self-contradictory phenomenon above may be qualitatively understood as follows: Though the eigensolutions are effectively not hybridized, propagation channels between the two chains are always present, allowing the information to possibly “propagate” from one chain to the other. To verify this picture, we first consider the system under OBCs with $\beta \rightarrow \infty$ and employ the Green's function to examine the interchain propagation in the bulk of the system, instead of the end-to-end response on one chain alone. Note that when the two chains are uncoupled, the spectra of the two chains under OBCs are real and partially overlapping due to their on-site potentials $V^{A,B}$ [see Fig. 2(a)]. Upon turning on the interchain coupling t_0 , a signal at one chain with frequency ω might propagate to the other chain. Such propagation is favored when both chains have eigenmodes sharing almost the same eigenenergy close to ω , satisfying the resonance condition. Therefore, an element from the Green's function related to the interchain response will be much larger for the input frequency ω falling in the central part of the spectrum than that for the frequency at the tails. This argument is confirmed by our numerical results for a loop response defined by

$$G_{\text{loop}} = G_{A_x, B_{x'}} G_{B_{x'}, A_x},$$

representing the product of two amplification ratios, one for a signal traveling from site x in chain A to site x' in chain B and the other vice versa, as shown in Fig. 2(b). More

¹For $|v_{\alpha}| > 1$, the single element shall be replaced by the determinant of its off-diagonal block when calculating the responses in Eq. (5) [21]

importantly, once a signal propagates to the other chain, it can be directionally amplified there, thus carrying over the winding topology of that chain before propagating back. In addition, these interchain propagating channels effectively form a propagation loop, and the signal traveling along the loop can be amplified repeatedly. This amplification mechanism can be interpreted as instabilities as well, hence the emergence of complex eigenenergies in the central part of the OBC spectrum, as shown in Fig. 2(a).

We now discuss why the boundary tuning parameter β makes a difference in our observations for G_{loop} , as seen in Figs. 2(b) and 2(c). First note that G_{loop} is related to signal amplification between two distanced lattice sites, which will vanish under PBCs [38,39]. Intuitively, boundary couplings $t_{\pm 1}^{A,B} e^{-\beta}$ connecting each chain head to tail also provide intra-chain propagation channels, which may be enhanced by the nonreciprocal pumping and overwhelm the interchain ones under weak interchain coupling, i.e., $t_0 < t_{\pm 1}^{A,B} e^{-\beta}$. Indeed, we see that G_{loop} is almost vanishing when the system is under PBCs ($\beta = 0$), as shown in Fig. 2(b). On the other hand, when the system is tuned away from the PBCs (i.e., increasing β from zero), G_{loop} becomes larger only for ω falling in the central part of the spectrum, where interchain propagations are favored due to resonances. In Fig. 2(c) we present G_{loop} for several different eigenenergies, and it is clearly seen that G_{loop} increases rapidly with β for eigenenergies in the central part of the spectrum. That is, for the parameters we consider, the propagation channels start to play a role when the system is slightly tuned away from the PBCs. The existence of such propagation channels allows the spectral topology of one chain, which is essentially a property under PBCs, to be revealed from the steady-state response defined on the other chain for a certain energy window, even when the eigensolutions are effectively not hybridized between the two chains.

V. TOPOLOGICAL RESPONSE AND ENTANGLEMENT ENTROPY

It remains to study in more depth the properties of the interchain propagation channels in the competition between interchain coupling t_0 and the boundary tuning parameter β . Figures 3(a) and 3(b) present the steady-state response defined in Eq. (5) on chain A alone for the reference energy $E_r = 0$, i.e., the center of the spectrum with $\mathbf{w}(E_r) = (1, -1)$. One sees $\nu_{\leftarrow}^A = 1$ (yellow regime) for a wide range of t_0 when β is below a certain β_{c1} in Fig. 3(a). This suggests that the eigensolutions are effectively not hybridized between the two chains. The other response ν_{\rightarrow}^A , shown in Fig. 3(b), is also quantized at $\nu_{\rightarrow}^A = 1$ (yellow regime), reflecting that the spectral winding of chain B can be probed from chain A in a subregime of the yellow regime in Fig. 3(a). We refer to the yellow regime in Fig. 3(b) as anomalous hybridization, which covers a rather large parameter space. Anomalous hybridization signifies that interchain propagation channels are favored, though eigensolutions are effectively not hybridized between the two chains. In addition, note that with a larger β , the system approaches the OBC limit with trivial spectral winding and hence always gives a trivial steady-state response. With this insight and previous results [24,41,42], we infer that the steady-state response considered here can distinguish between

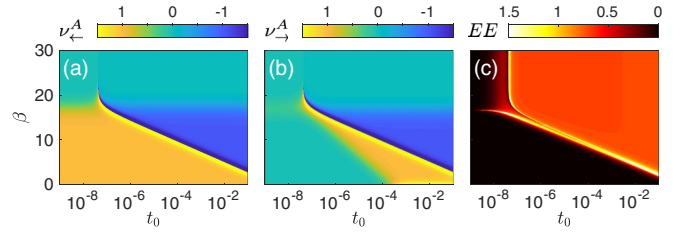


FIG. 3. Quantized steady-state responses defined on the A chain (a) ν_{\leftarrow}^A and (b) ν_{\rightarrow}^A for a reference energy at $E_r = 0$. The yellow area in (a) has a steady-state response with $\nu_{\leftarrow}^A = 1$, reflecting only the single-band winding number $w_+(0)$. Eigensolutions are effectively dehybridized between the two chains, which is further verified by the vanishing EE in (c). In (b) a subarea (yellow) of the dehybridization regime gives a steady-state response with $\nu_{\rightarrow}^A = 1$, suggesting an anomalous hybridization behavior with resonant interchain propagation channels. (c) Entanglement entropy for the N th eigenmode sorted in its real energy. The other parameters are $t_1^A = t_{-1}^B = 1$, $t_{-1}^A = t_1^B = 0.5$, $V^A = -V^B = 0.5$, and the system size $N = 50$.

dehybridization and anomalous hybridization regimes when $\beta < \beta_{\text{OBC}} \approx N \ln \sqrt{t_1^A/t_{-1}^A}$.

To further justify the dehybridization of the eigensolutions in the anomalous hybridization regime and verify our conjecture on the emergence of β_{c1} , we investigate the interchain entanglement entropy (EE) and compare the results with the quantized responses obtained. Specifically, we compute the biorthogonal EE for an entanglement cut chosen between the two chains, defined as [26,43,44]

$$S_n = - \sum_m \eta_{n,m} \ln \eta_{n,m} + (1 - \eta_{n,m}) \ln(1 - \eta_{n,m}), \quad (6)$$

where $\eta_{n,m}$ is the m th eigenvalue of the correlator matrix C_n for the n th eigenmode,

$$(C_n)_{xy} = \langle \Psi_n^L | \hat{c}_x^\dagger \hat{c}_y | \Psi_n^R \rangle, \quad (7)$$

with x, y from only chain A. In Fig. 3(c) we show the EE for the N th eigenmode (sorted by its real energy), which corresponds to the most pronounced G_{loop} in Figs. 2(b) and 2(c). The regime with $S_N \approx 0$ coincides well with the dehybridization regime, whereas the regime with $S_N \approx \ln 2$ corresponds to the hybridization regime found in Fig. 3(a). Notably, these two said regimes are seen to have sharp boundaries. That is, in the anomalous hybridization regime identified as the yellow area in Fig. 3(b), entanglement between the two chains is vanishing. This confirms again that the eigensolutions are effectively not hybridized.

VI. PHASE DIAGRAM

We finally present a phase diagram of our system based on the steady-state response and entanglement analysis in Fig. 4(a). The dehybridization regime is represented by the green area, where the single-chain spectral winding topology manifests itself as a quantized steady-state response on that chain alone. The anomalous hybridization regime is marked by the orange area, where eigensolutions are effectively not hybridized (vanishing entanglement between the two chain), while importantly interchain propagation channels allow the

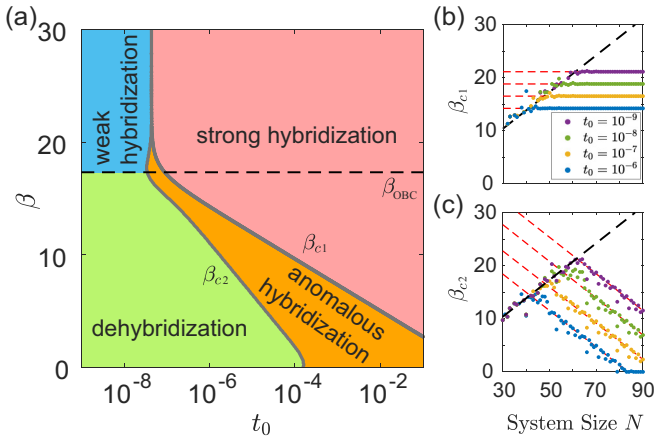


FIG. 4. (a) Phase diagram of the system read out from the quantized response quantities and EE in Fig. 3. Colors indicate different phases as labeled in the figure. The phase boundaries (b) β_{c1} and (c) β_{c2} vary with the system size N . The black dashed lines indicate $\beta_{\text{OBC}} \approx N \ln \sqrt{t_1^A/t_1^B}$, where the system approaches the OBC limit. The data points are read out from the jumps of the quantized response quantities $\nu_{\vec{a}}^A$. Red dash lines are the numerical fitting of the data points. The three critical values for a fixed N roughly cross each other at the same point, as further shown in the Supplemental Material [33]. The parameters are $t_1^A = t_1^B = 1$, $t_1^A = t_1^B = 0.5$, and $V^A = -V^B = 0.5$. Numerically we obtain $\beta_{c1} \approx \ln t_0$, which is also independent of the reference energy E_r [33].

spectral winding topology of one chain to be detected from the response defined on the other chain alone. The pink area represents a strong hybridization regime, where the interchain EE is saturated, and the steady-state response in this regime reflects the total spectral winding of the system for a reference energy when $\beta < \beta_{\text{OBC}}$. Finally, the blue area in Fig. 4(a) depicts a weak hybridization regime, where the EE decreases with t_0 as shown in Fig. 3(c). Both response quantities in Figs. 3(a) and 3(b) take a value of zero in this regime, since it falls in the OBC limit with $\beta > \beta_{\text{OBC}}$, where the spectral winding vanishes. Notably, the weak hybridization is consistent with the critical NHSE [26], where the OBC system in a weak regime of t_0 shows intermediate behaviors between hybridized and dehybridized scenarios of the two chains.

Our phase diagram highlights several transitions when increasing β from 0, e.g., with $t_0 = 10^{-5}$ for E_r with $\mathbf{w}(E_r) = (1, -1)$, including (i) a transition between the anomalous hybridization regime and strong hybridization at β_{c1} and (ii) a transition between the dehybridization regime and anomalous hybridization at β_{c2} . Another critical value β_{OBC} is known to be proportional to the system's size N [24,41,42], which indicates that the system behaves more like under OBCs with spectral winding vanishing. Interestingly, β_{c1} and β_{c2} are found to exhibit markedly different scaling with the system's size N , as shown in Figs. 4(b) and 4(c). That is, β_{c1} remains a constant as N varies, whereas β_{c2} decreases with increasing N (see the Supplemental Material [33] for more details). In summary, it is now evident that as the system's size increases, the anomalous hybridization regime (orange regime) bordered by the lines β_{c2} and β_{c1} widens. Hence the anomalous hybridization regime is approachable in a larger parameter space

when the system is taken to the thermodynamic limit. Indeed, it cannot be stressed enough that non-Hermitian systems can be extremely sensitive to couplings between boundaries or between different subsystems. The Supplemental Material [33] contains more detailed analysis of β_{c2} and β_{c1} by considering different specific values of the reference energy E_r .

VII. DIRECTIONAL SIGNAL PROPAGATION IN DRIVEN-DISSIPATIVE CAVITY ARRAY

The steady-state response has been introduced for the directional signal amplification process in various one-dimensional chains [21,38,39,45]. To experimentally realize our setup, we propose to consider coupling two driven-dissipative cavity arrays in Ref. [38] with coherent interchain couplings. The Hamiltonian and the master equation describing our proposed experimental system read

$$\begin{aligned} \hat{H}_0 &= \sum_x (J_a \hat{c}_{a,x}^\dagger \hat{c}_{a,x+1} + J_b \hat{c}_{b,x}^\dagger \hat{c}_{b,x+1} + J_0 \hat{c}_{a,x}^\dagger \hat{c}_{b,x} + \text{H.c.}) \\ &+ \sum_x (\mu_a \hat{c}_{a,N}^\dagger \hat{c}_{a,N} + \mu_b \hat{c}_{b,N}^\dagger \hat{c}_{b,N}) \\ &+ e^\beta (\hat{c}_{a,N}^\dagger \hat{c}_{a,N} + \hat{c}_{b,N}^\dagger \hat{c}_{b,N}), \\ \dot{\rho} &= -i[\hat{H}_0, \rho] + \sum_x \sum_{\alpha=a,b} (\Gamma_\alpha D[\hat{z}_{x,\alpha}] \rho \\ &+ \kappa D[\hat{c}_{x,\alpha}^\dagger] \rho + \gamma_\alpha D[\hat{c}_{x,\alpha}] \rho), \end{aligned} \quad (8)$$

with $D[\hat{z}_{x,\alpha}] \rho = \hat{z}_{x,\alpha} \rho \hat{z}_{x,\alpha}^\dagger - \frac{1}{2} \{\hat{z}_{x,\alpha}^\dagger \hat{z}_{x,\alpha}, \rho\}$ and $\hat{z}_{x,\alpha} = \hat{c}_{x,\alpha} + e^{-i\theta_\alpha} \hat{a}_{x+1,\alpha}$. Here J_α and J_0 are the amplitudes of intra-chain and interchain hoppings, respectively, with $\alpha = a$ or b ; $\Gamma_\alpha D[\hat{z}_{x,\alpha}] \rho$ describes dissipative couplings between neighbor sites; $\kappa D[\hat{c}_{x,\alpha}^\dagger] \rho$ describes a uniform local incoherent pumping of photons, which could drive the system into the regime with nontrivial spectral winding; and $\gamma_\alpha D[\hat{c}_{x,\alpha}] \rho$ describes photon decay into a waveguide coupled to each cavity, which also allows a signal to enter and exit the cavities. In addition, we introduce uniform local energy detuning $\mu_{a,b}$ on the two chains and an extra detuning e^β at the boundary for both chains [46,47]. The latter can effectively interpolate the boundary condition of the system from PBC to OBC, which is essential for the observation of the quantized steady-state response [45].

For an input field $\langle c_{x,\alpha}^{\text{in}}(t) \rangle$ entering the system, we can derive the equation of motion for the mean cavity amplitudes $\langle c_{x,\alpha} \rangle$ [33]. The input and output fields $\langle c_{x,\alpha}^{\text{in}}(\omega) \rangle$ and $\langle c_{x,\alpha}^{\text{out}}(\omega) \rangle$ at frequency ω are related by [38,48]

$$\mathbf{a}_{\text{out}} = \mathbf{a}_{\text{in}} - \frac{i\gamma}{\omega - H} \mathbf{a}_{\text{in}} = \mathbf{a}_{\text{in}} - i\gamma G \mathbf{a}_{\text{in}}, \quad (9)$$

with $\mathbf{a}_{\text{in/out}} = (\langle c_{1,a}^{\text{in/out}} \rangle, \dots, \langle c_{N,a}^{\text{in/out}} \rangle, \langle c_{1,b}^{\text{in/out}} \rangle, \dots, \langle c_{N,b}^{\text{in/out}} \rangle)^T$. Note that the Green's function G in Eq. (9) is defined with a real frequency ω , acting as the real part of the reference energy E_r in the previous discussion. Its imaginary part can be mimicked by a uniform local pumping of κ , which shifts the spectrum along the imaginary axis. Now let us investigate the steady-state response in the proposed system by consider a signal entering and leaving the system at different ends. For example, a signal traveling from $(1, a)$ to $(N-1, a)$ is

described by the expression

$$\langle c_{N-1,a}^{\text{out}} \rangle = -i\gamma G_{(N-1)a,1a} \langle c_{1,a}^{\text{in}} \rangle, \quad (10)$$

with $G_{(N-1)a,1a}$ an element of the Green's function. Note that the two ends of interest are now given by $x = 1$ and $x = N - 1$, as we have placed an energy detuning e^β at $x = N$. We can then map the effective Hamiltonian obtained above to our model (1), with the modifier $e^{-\beta}$ on the boundary couplings replaced by an extra local energy detuning e^β at site N for both chains. Qualitatively, we can observe that the quantity defined from the steady-state response jumps from a pseudoplateau to negative values when β exceeds a critical value β_{c1} , which verifies the anomalous hybridization in the coupled chain system. Numerically simulated results and more details are presented in the Supplemental Material [33].

VIII. CONCLUSION

Topological physics in non-Hermitian systems continues to surprise us. In investigating the probe of spectral winding topology through quantized steady-state responses to changes in boundary coupling, we revealed a counterintuitive

phenomenon in a non-Hermitian coupled chain setting. Even when the observed energetics and the entanglement entropy clearly indicate that the eigensolutions are effectively not hybridized, the spectral winding topology of one chain can be probed by a response defined on the other chain alone for a certain frequency of the input signal. Termed anomalous hybridization, this was explained by the dominance of the resonant interchain propagation channels over the intra-chain ones. This phenomenon was shown to be robust against disorder and emerge generally in several more sophisticated models with next-nearest-neighbor interchain couplings, coupled multiband chains, and/or higher winding numbers, as further discussed in the Supplemental Material [33].

ACKNOWLEDGMENTS

L.L. acknowledges financial support from the National Natural Science Foundation of China through Grant No. 12104519 and the Guangdong Basic and Applied Basic Research Foundation through Grant No. 2020A1515110773. J.G. acknowledges support from Singapore National Research Foundation through Grant No. NRF-NRFI2017-04 (WBS No. A-0004162-00-00). H.-Q.L. and S.M. contributed equally to this work.

-
- [1] K. Kawabata, K. Shiozaki, M. Ueda, and M. Sato, Symmetry and Topology in Non-Hermitian Physics, *Phys. Rev. X* **9**, 041015 (2019).
 - [2] H. Shen, B. Zhen, and L. Fu, Topological Band Theory for Non-Hermitian Hamiltonians, *Phys. Rev. Lett.* **120**, 146402 (2018).
 - [3] D. S. Borgnia, A. J. Kruchkov, and R.-J. Slager, Non-Hermitian Boundary Modes and Topology, *Phys. Rev. Lett.* **124**, 056802 (2020).
 - [4] N. Okuma, K. Kawabata, K. Shiozaki, and M. Sato, Topological Origin of Non-Hermitian Skin Effects, *Phys. Rev. Lett.* **124**, 086801 (2020).
 - [5] K. Zhang, Z. Yang, and C. Fang, Correspondence between Winding Numbers and Skin Modes in Non-Hermitian Systems, *Phys. Rev. Lett.* **125**, 126402 (2020).
 - [6] V. M. M. Alvarez, J. E. B. Vargas, and L. E. F. F. Torres, Non-Hermitian robust edge states in one dimension: Anomalous localization and eigenspace condensation at exceptional points, *Phys. Rev. B* **97**, 121401(R) (2018).
 - [7] S. Yao and Z. Wang, Edge States and Topological Invariants of Non-Hermitian Systems, *Phys. Rev. Lett.* **121**, 086803 (2018).
 - [8] K. Yokomizo and S. Murakami, Non-Bloch Band Theory of Non-Hermitian Systems, *Phys. Rev. Lett.* **123**, 066404 (2019).
 - [9] F. Song, S. Yao, and Z. Wang, Non-Hermitian Skin Effect and Chiral Damping in Open Quantum Systems, *Phys. Rev. Lett.* **123**, 170401 (2019).
 - [10] C. H. Lee, L. Li, and J. Gong, Hybrid Higher-Order Skin-Topological Modes in Nonreciprocal Systems, *Phys. Rev. Lett.* **123**, 016805 (2019).
 - [11] C. H. Lee and R. Thomale, Anatomy of skin modes and topology in non-Hermitian systems, *Phys. Rev. B* **99**, 201103(R) (2019).
 - [12] C. H. Lee, L. Li, R. Thomale, and J. Gong, Unraveling non-Hermitian pumping: Emergent spectral singularities and anomalous responses, *Phys. Rev. B* **102**, 085151 (2020).
 - [13] L. Li, C. H. Lee, and J. Gong, Topological Switch for Non-Hermitian Skin Effect in Cold-Atom Systems with Loss, *Phys. Rev. Lett.* **124**, 250402 (2020).
 - [14] Y. Yi and Z. Yang, Non-Hermitian Skin Modes Induced by On-Site Dissipations and Chiral Tunneling Effect, *Phys. Rev. Lett.* **125**, 186802 (2020).
 - [15] T. Helbig, T. Hofmann, S. Imhof, M. Abdelghany, T. Kiessling, L. W. Molenkamp, C. H. Lee, A. Szameit, M. Greiter, and R. Thomale, Generalized bulk-boundary correspondence in non-Hermitian topoelectrical circuits, *Nat. Phys.* **16**, 747 (2020).
 - [16] L. Xiao, T. Deng, K. Wang, G. Zhu, Z. Wang, W. Yi, and P. Xue, Non-Hermitian bulk-boundary correspondence in quantum dynamics, *Nat. Phys.* **16**, 761 (2020).
 - [17] A. Ghatak, M. Brandenbourger, J. van Wezel, and C. Coullais, Observation of non-Hermitian topology and its bulk-edge correspondence in an active mechanical metamaterial, *Proc. Natl. Acad. Sci. USA* **117**, 29561 (2020).
 - [18] K. Wang, A. Dutt, K. Y. Yang, C. C. Wojcik, J. Vučković, and S. Fan, Generating arbitrary topological windings of a non-Hermitian band, *Science* **371**, 1240 (2021).
 - [19] L. Zhang, Y. Yang, Y. Ge, Y.-J. Guan, Q. Chen, Q. Yan, F. Chen, R. Xi, Y. Li, D. Jia, S.-Q. Yuan, H.-X. Sun, H. Chen, and B. Zhang, Acoustic non-Hermitian skin effect from twisted winding topology, *Nat. Commun.* **12**, 6297 (2021).
 - [20] R. Su, E. Estrecho, D. Biegańska, Y. Huang, M. Wurdack, M. Pieczarka, A. G. Truscott, T. C. H. Liew, E. A. Ostrovskaya, and Q. Xiong, Direct measurement of a non-Hermitian topological invariant in a hybrid light-matter system, *Sci. Adv.* **7**, eabj8905 (2021).

- [21] L. Li, S. Mu, C. H. Lee, and J. Gong, Quantized classical response from spectral winding topology, *Nat. Commun.* **12**, 5294 (2021).
- [22] J. C. Budich and E. J. Bergholtz, Non-Hermitian Topological Sensors, *Phys. Rev. Lett.* **125**, 180403 (2020).
- [23] A. McDonald and A. A. Clerk, Exponentially-enhanced quantum sensing with non-Hermitian lattice dynamics, *Nat. Commun.* **11**, 5382 (2020).
- [24] L. Li, C. H. Lee, and J. Gong, Impurity induced scale-free localization, *Commun. Phys.* **4**, 42 (2021).
- [25] C.-X. Guo, C.-H. Liu, X.-M. Zhao, Y. Liu, and S. Chen, Exact Solution of Non-Hermitian Systems with Generalized Boundary Conditions: Size-Dependent Boundary Effect and Fragility of the Skin Effect, *Phys. Rev. Lett.* **127**, 116801 (2021).
- [26] L. Li, C. H. Lee, S. Mu, and J. Gong, Critical non-Hermitian skin effect, *Nat. Commun.* **11**, 5491 (2020).
- [27] C.-H. Liu, K. Zhang, Z. Yang, and S. Chen, Helical damping and dynamical critical skin effect in open quantum systems, *Phys. Rev. Research* **2**, 043167 (2020).
- [28] S. Mu, L. Zhou, L. Li, and J. Gong, Non-Hermitian pseudo mobility edge in a coupled chain system, *Phys. Rev. B* **105**, 205402 (2022).
- [29] J. Wiersig, Enhancing the Sensitivity of Frequency and Energy Splitting Detection by Using Exceptional Points: Application to Microcavity Sensors for Single-Particle Detection, *Phys. Rev. Lett.* **112**, 203901 (2014).
- [30] H. Hodaei, A. U. Hassan, S. Wittek, H. Garcia-Gracia, R. El-Ganainy, D. N. Christodoulides, and M. Khajavikhan, Enhanced sensitivity at higher-order exceptional points, *Nature (London)* **548**, 187 (2017).
- [31] W. Chen, Ş. K. Özdemir, G. Zhao, J. Wiersig, and L. Yang, Exceptional points enhance sensing in an optical microcavity, *Nature (London)* **548**, 192 (2017).
- [32] N. Hatano and D. R. Nelson, Localization Transitions in Non-Hermitian Quantum Mechanics, *Phys. Rev. Lett.* **77**, 570 (1996).
- [33] See Supplemental Material at <http://link.aps.org/supplemental/10.1103/PhysRevB.105.L241402> for (i) additional results on the quantized steady-state responses with different parameters, (ii) further discussion about the phase boundaries of β_{c1} and β_{c2} , (iii) results with weak hopping disorder, (iv) additional results on the quantized steady-state responses for different models, and (v) more details and numerical simulation of our experimental proposal of driven-dissipative cavity arrays.
- [34] J. Claes and T. L. Hughes, Skin effect and winding number in disordered non-Hermitian systems, *Phys. Rev. B* **103**, L140201 (2021).
- [35] W. P. Su, J. R. Schrieffer, and A. J. Heeger, Solitons in Polyacetylene, *Phys. Rev. Lett.* **42**, 1698 (1979).
- [36] Z. Gong, Y. Ashida, K. Kawabata, K. Takasan, S. Higashikawa, and M. Ueda, Topological Phases of Non-Hermitian Systems, *Phys. Rev. X* **8**, 031079 (2018).
- [37] A. McDonald, T. Pereg-Barnea, and A. A. Clerk, Phase-Dependent Chiral Transport and Effective Non-Hermitian Dynamics in a Bosonic Kitaev-Majorana Chain, *Phys. Rev. X* **8**, 041031 (2018).
- [38] C. C. Wanjura, M. Brunelli, and A. Nunnenkamp, Topological framework for directional amplification in driven-dissipative cavity arrays, *Nat. Commun.* **11**, 3149 (2020).
- [39] W.-T. Xue, M.-R. Li, Y.-M. Hu, F. Song, and Z. Wang, Simple formulas of directional amplification from non-Bloch band theory, *Phys. Rev. B* **103**, L241408 (2021).
- [40] In one-dimensional non-Hermitian systems, the complex variable $E_+(k) - E_-(k)$ is generally nonzero since k is scalar.
- [41] R. Koch and J. C. Budich, Bulk-boundary correspondence in non-Hermitian systems: Stability analysis for generalized boundary conditions, *Eur. Phys. J. D* **74**, 70 (2020).
- [42] F. K. Kunst, E. Edvardsson, J. C. Budich, and E. J. Bergholtz, Biorthogonal Bulk-Boundary Correspondence in Non-Hermitian Systems, *Phys. Rev. Lett.* **121**, 026808 (2018).
- [43] P.-Y. Chang, J.-S. You, X. Wen, and S. Ryu, Entanglement spectrum and entropy in topological non-Hermitian systems and nonunitary conformal field theory, *Phys. Rev. Research* **2**, 033069 (2020).
- [44] L. Li and C. H. Lee, Non-Hermitian pseudo-gaps, *Sci. Bull.* **67**, 685 (2022).
- [45] Y. Liu, Y. Zeng, L. Li, and S. Chen, Exact solution of the single impurity problem in nonreciprocal lattices: Impurity-induced size-dependent non-Hermitian skin effect, *Phys. Rev. B* **104**, 085401 (2021).
- [46] L. Zhou, Z. R. Gong, Y.-x. Liu, C. P. Sun, and F. Nori, Controllable Scattering of a Single Photon inside a One-Dimensional Resonator Waveguide, *Phys. Rev. Lett.* **101**, 100501 (2008).
- [47] C. Derntl, M. Schneider, J. Schalko, A. Bittner, J. Schmiedmayer, U. Schmid, and M. Trupke, Arrays of open, independently tunable microcavities, *Opt. Express* **22**, 22111 (2014).
- [48] C. C. Wanjura, M. Brunelli, and A. Nunnenkamp, Correspondence between Non-Hermitian Topology and Directional Amplification in the Presence of Disorder, *Phys. Rev. Lett.* **127**, 213601 (2021).